2014

Effect of Superhydrophobic Surface Morphology on Evaporative Deposition Patterns

M. Dicuangco
Purdue University

S. Dash
Purdue University

J. A. Weibel
Purdue University, jaweibel@purdue.edu

S. V. Garimella
Purdue University, sureshg@purdue.edu

Dicuangco, M.; Dash, S.; Weibel, J. A.; and Garimella, S. V., "Effect of Superhydrophobic Surface Morphology on Evaporative Deposition Patterns" (2014). *CTRC Research Publications.* Paper 221.
http://dx.doi.org/dx.doi.org/10.1063/1.4878322

Effect of superhydrophobic surface morphology on evaporative deposition patterns

Mercy Dicuangco, Susmita Dash, Justin A. Weibel, and Suresh V. Garimella[a)]
School of Mechanical Engineering, Purdue University, West Lafayette, Indiana 47907, USA

(Received 25 March 2014; accepted 5 May 2014; published online 22 May 2014)

Prediction and active control of the spatial distribution of particulate deposits obtained from sessile droplet evaporation are vital in printing, nanostructure assembly, biotechnology, and other applications that require localized deposits. This Letter presents surface wettability-based localization of evaporation-driven particulate deposition and the effect of superhydrophobic surface morphology on the distribution of deposits. Sessile water droplets containing suspended latex particles are evaporated on non-wetting textured surfaces with varying microstructure geometry at ambient conditions. The droplets are visualized throughout the evaporation process to track the temporal evolution of contact radius and apparent contact angle. The resulting particle deposits on the substrates are quantitatively characterized. The experimental results show that superhydrophobic surfaces suppress contact-line deposition during droplet evaporation, thereby providing an effective means of localizing the deposition of suspended particles. A correlation between deposit size and surface morphology, explained in terms of the interface pressure balance at the transition between wetting states, reveals an optimum surface morphology for minimizing the deposit coverage area. © *2014 AIP Publishing LLC*. [http://dx.doi.org/10.1063/1.4878322]

Tunable deposit patterns obtained from droplet evaporation are desirable in a variety of applications. Evaporative patterning of functional nanomaterials, including nanowires[1] and gold nanoparticles,[2,3] has become instrumental in developing nanomaterial-based optoelectronic devices.[4] DNA microarrays,[5,6] biosensors,[7–9] and protein delivery systems[10] rely on localized, evaporative deposition to detect and analyze biological materials. For processes that require uniform particulate deposits from inkjet-printed droplets, the effects of particle concentration[11] and solvent composition[11,12] have been studied to eliminate undesirable ring-like patterns.

An understanding of the droplet evaporation behavior is essential in order to control spatial distribution of deposits. On smooth surfaces, researchers have demonstrated control over the formation of ring-like, centralized, and uniform deposit patterns. Deegan *et al.*[13,14] ascribed ring-like deposits (the "coffee-ring" effect) to capillary-driven flow of particles to the pinned contact line, where the local evaporation rate was highest. Popov[15] evaluated the theoretical growth rates and sizes of such ring deposits as a function of initial solute concentration using a closed-form solution that assumed a pinned contact line. Annular deposits have also been experimentally observed in the interior of the initial droplet footprint by Nguyen *et al.*[16] due to pinning of the contact line at later stages of evaporation. Factors affecting secondary contact line pinning (viz., surface roughness/wettability, particulate shape, and salt concentration) controlled the size and configuration of these inner coffee-ring deposits. Hu and Larson[17] first described particle deposition at the center of the droplet after dry-out and attributed this to the strengthened recirculating Marangoni flow in organic liquids that prevented particles from accumulating at the contact line. Ristenpart *et al.*[18] demonstrated that tuning the direction of Marangoni flow allowed controlled distribution of the deposits. A phase diagram of deposition patterns was later developed by Bhardwaj *et al.*[19] based on the competition between capillary-driven flow, Marangoni flow, and electrostatic/intermolecular force-driven particle assembly.

Droplet evaporation on superhydrophobic (SH) surfaces[20–22] has received growing attention; however, there are no standard measures to characterize and predict the size and location of deposits on rough surfaces with non-wetting properties. In recent studies,[23–25] the droplet evaporation rate was reported to be reduced on superhydrophobic surfaces due to increased influence of evaporative cooling at the droplet interface. Three modes of droplet evaporation on superhydrophobic surfaces have been reported[20,26,27] as well: a constant contact radius (CCR) mode, a constant contact angle (CCA) mode, and a mixed mode. In the CCR mode, the contact line remains pinned while the contact angle decreases, whereas in the CCA mode, the contact angle remains fixed as the contact line recedes. The droplet contact radius and contact angle decrease simultaneously in the mixed mode. In a previous visualization study,[28] evaporative deposition on superhydrophobic surfaces resulted in deposit areas significantly smaller than the initial droplet base area. Deposits were localized due to continuous contact line recession until the late stages of evaporation; the deposit distribution was not correlated to surface morphology. On a highly non-wetting microtextured surface, Brunet[29] observed localized deposits with sizes dependent on the initial particle concentration and droplet volume. Marin *et al.*[30] demonstrated the ability to deposit a spherical cluster of particles on a superhydrophobic surface due to the receding contact line. Ebrahimi *et al.*,[7] Tirinato *et al.*,[8] and De Angelis *et al.*[9] used superhydrophobic surfaces to facilitate dense packing of molecular deposits for improved nanosensor efficiency/sensitivity.

[a)]Electronic mail: sureshg@purdue.edu. Tel.: (765) 494-5621

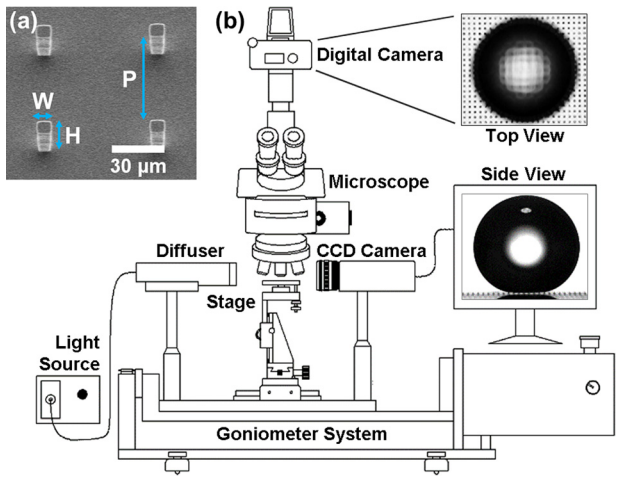

FIG. 1. (a) SEM image of representative pillar array unit cell (SH-65) and (b) schematic diagram of test facility.

We investigate the influence of superhydrophobic surface morphology on evaporative deposition by employing microstructured surfaces with differing pillar pitch as a mean to control the size and localization of particle deposits. Microliter droplets containing suspensions of latex microspheres are evaporated under ambient temperature and humidity conditions, and the resulting evaporative deposition patterns are analyzed. The deposit size dependence on surface morphology and transient evaporation dynamics are demonstrated experimentally and corroborated with theoretical analysis of transition between the predominant wetting states.

Superhydrophobicity may be imparted by engineering nano-, micro-, or multi-scale hydrophobic roughness elements on a substrate.[21] In the present work, five different superhydrophobic surfaces are designed with Teflon-coated, microscale pillars that offer a range of wetting characteristics as predicted by the global minimum energy.[31] The design procedure and fabrication of the surfaces are further discussed in the supplementary material.[32] Figure 1(a) shows a scanning electron microscopy (SEM) image of a representative pillar unit cell in which the parametric geometries are defined. The pillar width (W) and height (H) are fixed at 10 μm and 20 μm, respectively. Surface wettability is then a function of the pillar pitch (P), which takes values of 20 μm, 25 μm, 30 μm, 45 μm, and 65 μm; the surfaces are differentiated by pitch with a notation format of SH-P.

TABLE I. Theoretical[32] and measured static contact angles, and number of droplet evaporation trials, for each surface.

Surface (SH-P[a])	Theoretical Cassie state contact angle[32] (deg)	Theoretical Wenzel state contact angle[32] (deg)	Measured static contact angle (deg)	Number of trials
SH-20	151	180	151.5 ± 2.2	7
SH-25	157	180	154.5 ± 1.5	11
SH-30	161	161	156.9 ± 1.3	7
SH-45	134	167	156.5 ± 6.1	6
SH-65	127	171	161.7 ± 1.7	12

[a]SH-P is the superhydrophobic surface with pitch P (in μm).

A uniform suspension of particles in deionized water (0.002% mass concentration) is prepared with 1 μm-diameter latex microspheres that have a density of 1.05 g/cm^3 which ensures that they follow the flow field.[33] The experimental apparatus illustrated in Figure 1(b) is utilized to perform droplet evaporation tests with ambient temperature and relative humidity maintained at 21.6 ± 0.6 °C and 36.1 ± 0.9%, respectively. For each evaporation trial, a 3 μl droplet is gently deposited on the test surface using a microsyringe. Droplet profile distortion due to gravitational effects can be neglected since the diameter of the droplet (1.79 mm) is less than the capillary length scale of water (2.7 mm). Images of the side-view droplet profile, and measurements of the droplet contact angle and contact radius, are gathered at 1 s intervals with a goniometer system (Ramé-Hart, model 290), which uses a cold light source for background image contrast and does not influence the evaporation rate. The droplet profile is simultaneously recorded from atop via microscopy

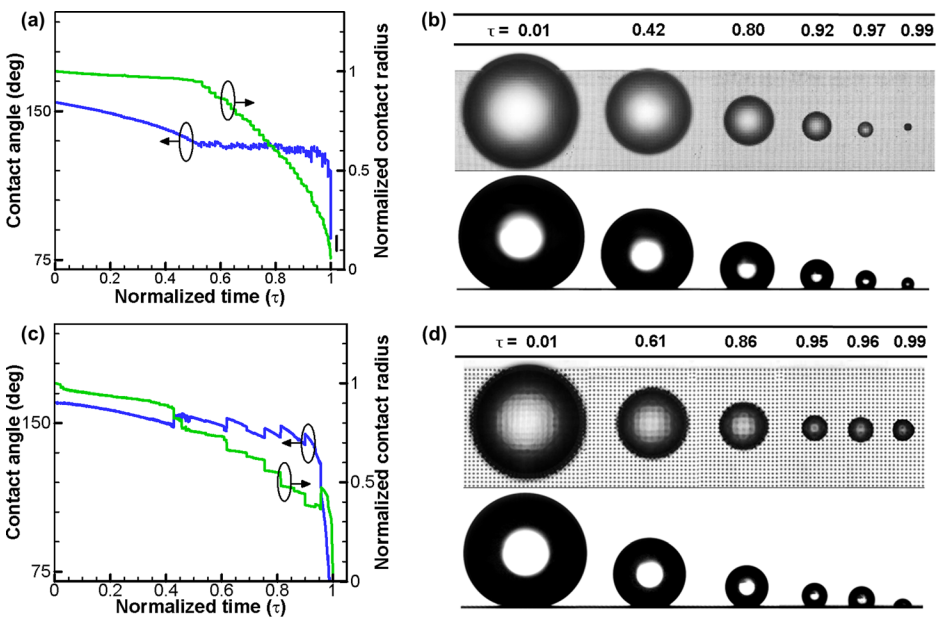

FIG. 2. Temporal variation of droplet contact angle and normalized contact radius on (a) SH-25 and (c) SH-65 for a single representative trial, and corresponding top- and side-view images of the droplet on (b) SH-25 and (d) SH-65.

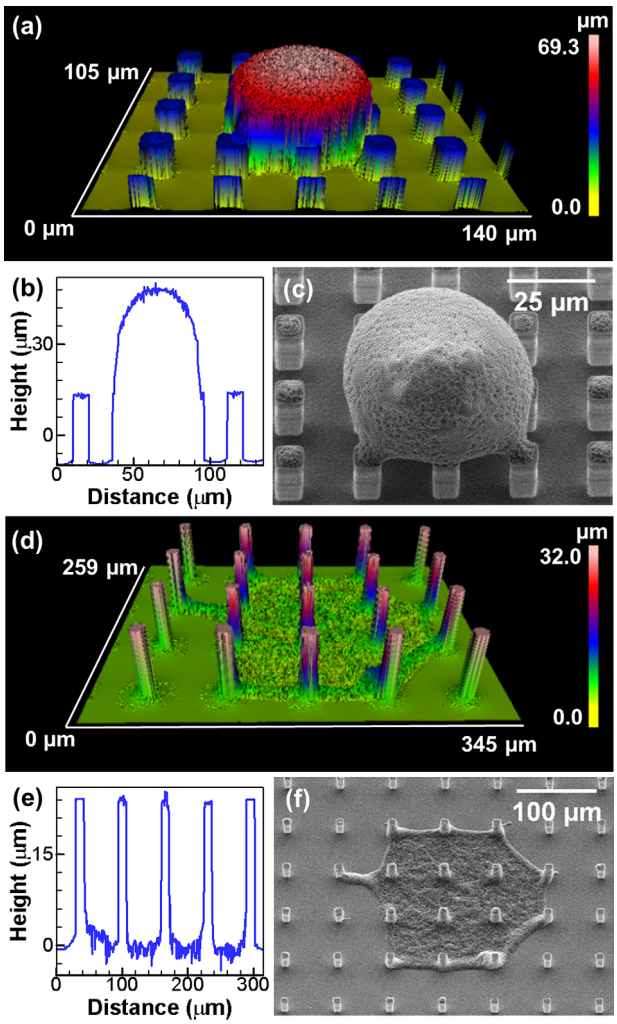

FIG. 3. (a) and (d) Three-dimensional representations of surface height topography and (b) and (e) surface profiles (along one cross-plane) obtained by optical interferometry, and (c) and (f) SEM images of the deposited particles, for surfaces SH-25 (top) and SH-65 (bottom).

(5× objective). A fresh location on the surface is designated for each droplet evaporation trial, so as not to disturb deposits on the surface between subsequent trials. Table I lists the number of trials performed for each surface type, as well as the corresponding predicted[32] and measured average static contact angles. Irrespective of whether a surface was designed[32] to form droplets in a Cassie[34] or a Wenzel[35] state based on its pillar dimensions, gentle placement of the droplet atop the pillars always yielded a droplet in the Cassie state for the five test surfaces. He *et al.*[31] observed this same behavior when droplets were gently positioned, in contrast to the Wenzel state being attained when the droplets were released from a height.

Grayscale images and topographic maps of the particle deposits are obtained via white-light optical interferometry (NewView 6200, Zygo). The grayscale images are analyzed to measure the deposit perimeter and plan-view coverage area. An oblique view of the deposit morphology is provided by SEM.

Figure 2(a) (SH-25) and Figure 2(c) (SH-65) illustrate the temporal variation of droplet contact angle and contact radius for a representative trial in terms of nondimensional time, τ, normalized by the total evaporation time. Corresponding top- and side-view images of the instantaneous droplet profile are displayed in Figures 2(b) and 2(d). At the start of evaporation on SH-25, initially in the CCR mode, the droplet is in the nonwetting Cassie state and has a contact angle of 154.6° The contact line de-pins at $\tau \approx 0.53$, marking the onset of the CCA mode in which the contact angle is constant at $\sim 131.3 \pm 2.5°$; the contact radius continuously recedes until $\tau \approx 0.99$. This is followed by the final stage of evaporation where the contact radius and the contact angle simultaneously decrease until complete dryout. On the other hand, the evaporation process on the surface with the largest pillar pitch (SH-65) is observed to start in either a mixed mode (such as in the representative case in Figures 2(c) and 2(d) or in the CCR mode, as explained in greater detail in supplementary material.[32] In Figure 2(c), the droplet begins to evaporate with an initial contact angle of 160.5°. For $0.43 \lesssim \tau \lesssim 0.90$, the contact radius recedes as the contact line abruptly pins and de-pins repeatedly to maintain an average contact angle of $\sim 148.9 \pm 3.4°$. This stick-slip phenomenon[26] is characteristic of the sparser pillar geometry in the CCA mode. Near the end of evaporation ($\tau \approx 0.90$), the droplet returns to the mixed mode, and at $\tau \approx 0.96$, the contact radius experiences a sudden increase, signifying that the droplet has been impaled by the pillars and displaced the air gaps, entering the Wenzel state. This behavior agrees with surface structures in the literature[36] with similar pillar density.

The deposited particle distributions on SH-25 and SH-65 corresponding to the representative trials in Figure 2 are presented in Figure 3. It is evident from the measured deposit topography for SH-25 (Figures 3(a) and 3(b)) that densely packed particles are deposited on this surface, covering a footprint area that is ~0.61% of the initial droplet base coverage area. The deposit rests only on top of the pillars as shown in the SEM image from a tilted view (Figure 3(c)). This implies that the droplet remained in the Cassie state throughout the evaporation process, consistent with observations by Brunet.[30] In contrast, Figures 3(d)–3(f) reveal a "Wenzel deposit" in between the pillars on SH-65, which is indicative of the Cassie-to-Wenzel transition observed in Figures 2(c) and 2(d). The deposit coverage area is 11.7% of

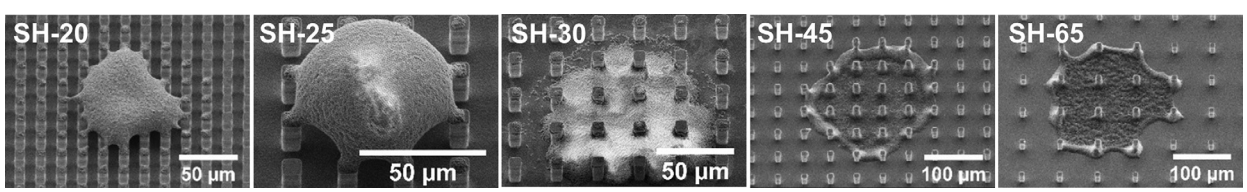

FIG. 4. SEM images of representative particulate deposits on the five surfaces investigated.

TABLE II. Ratio of deposit coverage area to the initial droplet base area (averaged across trials).

Surface (SH-P[a])	A_d[b]/A_i[c] (%)
SH-20	1.5 ± 0.62
SH-25	0.9 ± 0.30
SH-30	3.4 ± 0.56
SH-45	8.2 ± 5.51
SH-65	14.8 ± 6.98

[a]SH-P is the superhydrophobic surface with pitch P (in μm).
[b]A_d is the deposit coverage area.
[c]A_i is the initial droplet base area.

the initial droplet base coverage area and is significantly larger than the "Cassie deposit" on SH-25.

SEM images of representative deposits for all the surfaces in Figure 4 show the influence of surface morphology on deposit pattern. Cassie deposits are observed on SH-20 and SH-25, whereas Wenzel deposits are found on SH-30, SH-45, and SH-65. The Cassie-to-Wenzel transition is driven by the competition between the Laplace and capillary pressures, while a droplet is evaporating on the textured surface.[1,26,37] The Laplace pressure can be expressed as $P_L = 2\gamma/R$, where γ is the liquid surface tension and R is the droplet curvature radius; P_L increases as the droplet size decreases. The capillary pressure is defined as $P_C = -4\gamma(\cos\theta_Y)[\varphi/(W(1-\varphi))]$, where θ_Y is the Young's contact angle (120° for a water droplet on a smooth, Teflon-coated surface) and $\varphi = W^2/P^2$ is the surface solid fraction.[20] The capillary pressure decreases with increase in the pillar pitch. Cassie-to-Wenzel transition occurs when the droplet becomes small enough such that the Laplace pressure exceeds the capillary pressure ($P_L \geq P_C$); the deposition morphology (i.e., Cassie versus Wenzel deposits) is determined by this transition. A Wenzel deposit is formed for the surfaces on which transition is observed, viz., SH-65 as explained in the analysis of the time-dependent contact radius (Figure 2(c)), and SH-30 and SH-45 by viewing from atop per the discussion in the supplementary material.[32]

Table II provides a quantitative measure for the localization of deposits at the center of the droplets for all the test surfaces. The ratio of the deposit coverage area, A_d, to the initial droplet base area, A_i, is in the range of 0.87%–14.8%, indicating significant concentration of particles on all surfaces. Figure 5(a) shows a plot of A_d as a function of the pillar pitch. As the pillar pitch decreases, the particulate deposit coverage area reduces until a critical pitch (SH-25), below which the deposit size no longer continues to decrease with further decreases in pitch. On SH-20, the deposit coverage area is slightly larger than the observed minimum deposit size on SH-25. Xu *et al.*[1] observed a decreasing deposit area for three superhydrophobic surfaces with reducing pillar pitches; however, they did not investigate pillars dense enough to reveal a minimum achievable deposit size.

These observed trends in deposit size can be explained by the Laplace-capillary pressure balance at the wetting transition which is a function of the surface morphology. In Figure 5(a), it is clear that the trend of variation of A_d with pillar pitch follows the trend of the droplet base coverage area at wetting transition, A_t, obtained from top-view images just after transition for SH-30, SH-45, and SH-65. The deposit size can be correlated to the theoretical droplet curvature radius at Cassie-to-Wenzel transition, $R_t = 2\gamma/P_C$, as predicted by equating the Laplace and capillary pressures. Comparison to the measured curvature radius (Figure 5(b)) obtained from side-view images just prior to transition indicates that above the critical pillar pitch ($P > 25\ \mu$m) the wetting transition and deposit size are indeed governed by this Laplace-capillary pressure balance. While the theoretical curvature radius is able to broadly predict the measured wetting transition behavior trend with decreasing pillar pitch, the disagreement with experimental values shown in Figure 5(b) is expected due to the presence of particles in the fluid that influence the contact-line dynamics during droplet evaporation.[38–40] Above the critical pitch, Wenzel deposits are formed with a coverage area that is correlated to the droplet size predicted at Cassie-Wenzel transition, though the deposit coverage area is actually smaller than the droplet base coverage area at transition (Figure 5(a)). Below the critical pillar pitch ($P < 25\ \mu$m), the trend in deposit size no longer follows the trend in R_t (Figure 5(b)). At this threshold, the droplets remain in a Cassie state throughout evaporation. There is more significant influence of contact-line adhesion forces for surfaces with comparatively larger solid-liquid contact area between the droplet and the pillars,[41] which play a significant role toward the end of droplet evaporation; thus, further increase in pillar density act to increase the deposit size.

Evaporative particle deposition patterns and deposit sizes were studied as a function of superhydrophobic surface morphology. Droplet evaporation on superhydrophobic surfaces localizes particle deposition to an area significantly smaller than the initial base coverage area of the droplet. One of two types of deposition patterns is observed—Cassie or Wenzel deposits—corresponding to the droplet wetting

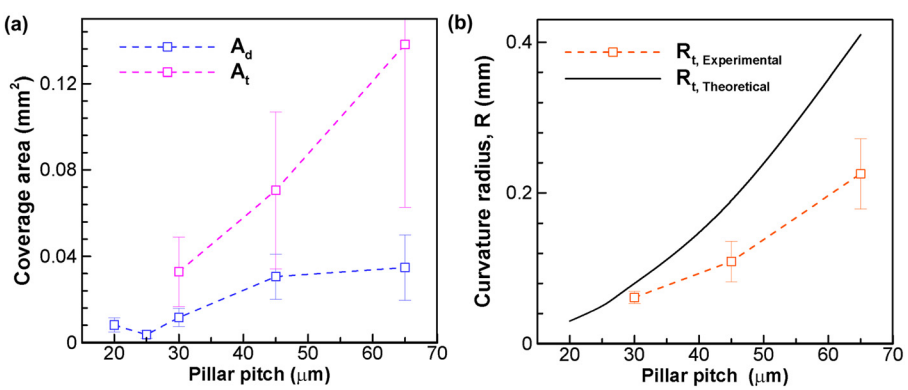

FIG. 5. (a) Measured deposit coverage area, A_d, and droplet base coverage area at Cassie-to-Wenzel transition, A_t, with respect to pillar pitch, and (b) comparison between the measured and theoretical droplet radius of curvature at Cassie-to-Wenzel transition, R_t.

state during the late stages of evaporation and is governed by a balance between the Laplace and capillary pressures. Over the range of surface geometries considered, a minimum average deposit size as small as 0.9% of the initial droplet base area is observed at a critical pillar pitch. Above the critical pitch, the deposit size is inversely proportional to the capillary pressure; the influence of contact-line adhesion forces dominates during the final stage of the evaporation process below this critical pitch. The present findings offer fundamental insights on controllable particulate deposition by droplet evaporation on superhydrophobic surfaces.

[1]W. Xu, R. Leeladhar, Y.-T. Tsai, E.-H. Yang, and C.-H. Choi, Appl. Phys. Lett. **98**, 073101 (2011).
[2]S. Liu, T. Zhu, R. Hu, and Z. Liu, Phys. Chem. Chem. Phys. **4**, 6059 (2002).
[3]T. P. Bigioni, X.-M. Lin, T. T. Nguyen, E. I. Corwin, T. A. Witten, and H. M. Jaeger, Nature Mater. **5**, 265 (2006).
[4]R. Yan, D. Gargas, and P. Yang, Nat. Photonics **3**, 569 (2009).
[5]G. Ciasca, L. Businaro, M. Papi, A. Notargiacomo, M. Chiarpotto, A. D. Ninno, V. Palmieri, S. Carta, E. Giovine, A. Gerardino, and M. D. Spirito, Nanotechnology **24**, 495302 (2013).
[6]V. Dugas, J. Broutin, and E. Souteyrand, Langmuir **21**, 9130 (2005).
[7]A. Ebrahimi, P. Dak, E. Salm, S. Dash, S. V. Garimella, R. Bashir, and M. A. Alam, Lab Chip **13**, 4248 (2013).
[8]L. Tirinato, F. Gentile, D. Di Mascolo, M. L. Coluccio, G. Das, C. Liberale, S. A. Pullano, G. Perozziello, M. Francardi, A. Accardo, F. De Angelis, P. Candeloro, and E. Di Fabrizio, Microelectron. Eng. **97**, 337 (2012).
[9]F. D. Angelis, F. Gentile, F. Mecarini, G. Das, M. Moretti, P. Candeloro, M. L. Coluccio, G. Cojoc, A. Accardo, C. Liberale, R. P. Zaccaria, G. Perozziello, L. Tirinato, A. Toma, G. Cuda, R. Cingolani, and E. Di Fabrizio, Nat. Photonics **5**, 682 (2011).
[10]H. Zhu and M. Snyder, Curr. Opin. Chem. Biol. **7**, 55 (2003).
[11]J. Park and J. Moon, Langmuir **22**, 3506 (2006).
[12]B.-J. de Gans and U. S. Schubert, Langmuir **20**, 7789 (2004).
[13]R. D. Deegan, O. Bakajin, T. F. Dupont, G. Huber, S. R. Nagel, and T. A. Witten, Phys. Rev. E **62**, 756 (2000).
[14]R. D. Deegan, O. Bakajin, T. F. Dupont, G. Huber, S. R. Nagel, and T. A. Witten, Nature **389**, 827 (1997).
[15]Y. O. Popov, Phys. Rev. E **71**, 036313 (2005).
[16]T. A. H. Nguyen, M. A. Hampton, and A. V. Nguyen, J. Phys. Chem. C **117**, 4707 (2013).
[17]H. Hu and R. G. Larson, J. Phys. Chem. B **110**, 7090 (2006).
[18]W. Ristenpart, P. Kim, C. Domingues, J. Wan, and H. Stone, Phys. Rev. Lett. **99**, 234502 (2007).
[19]R. Bhardwaj, X. Fang, P. Somasundaran, and D. Attinger, Langmuir **26**, 7833 (2010).
[20]S. Dash, M. T. Alt, and S. V. Garimella, Langmuir **28**, 9606 (2012).
[21]S. Dash, N. Kumari, and S. V. Garimella, J. Micromech. Microeng. **21**, 105012 (2011).
[22]Y. Kwon, N. Patankar, J. Choi, and J. Lee, Langmuir **25**, 6129 (2009).
[23]S. Dash and S. V. Garimella, Langmuir **29**, 10785 (2013).
[24]Z. Pan, S. Dash, J. A. Weibel, and S. V. Garimella, Langmuir **29**, 15831 (2013).
[25]S. Dash and S. V. Garimella, Phys. Rev. E **89**, 042402 (2014).
[26]W. Xu, R. Leeladhar, Y. T. Kang, and C.-H. Choi, Langmuir **29**, 6032 (2013).
[27]G. McHale, S. Aqil, N. J. Shirtcliffe, M. I. Newton, and H. Y. Erbil, Langmuir **21**, 11053 (2005).
[28]M. Dicuangco, S. Dash, and S. V. Garimella, J. Heat Transfer **135**, 080904 (2013).
[29]P. Brunet, Soft Matter **8**, 11294 (2012).
[30]A. G. Marin, H. Gelderblom, A. Susarrey-Arce, A. van Houselt, L. Lefferts, J. G. E. Gardeniers, D. Lohse, and J. H. Snoeijer, Proc. Natl. Acad. Sci. U.S.A. **109**, 16455 (2012).
[31]B. He, N. A. Patankar, and J. Lee, Langmuir **19**, 4999 (2003).
[32]See supplementary material at http://dx.doi.org/10.1063/1.4878322 for surface design and fabrication methods, analysis of the time-dependent contact angle/radius during evaporation, and observations of wetting state transition.
[33]A. Melling, Meas. Sci. Technol. **8**, 1406 (1997).
[34]A. B. D. Cassie and S. Baxter, Trans. Faraday Soc. **40**, 546 (1944).
[35]R. N. Wenzel, Ind. Eng. Chem. **28**, 988 (1936).
[36]P. Papadopoulos, L. Mammen, X. Deng, D. Vollmer, and H.-J. Butt, Proc. Natl. Acad. Sci. U.S.A. **110**, 3254 (2013).
[37]C. Antonini, J. B. Lee, T. Maitra, S. Irvine, D. Derome, M. K. Tiwari, J. Carmeliet, and D. Poulikakos, Sci. Rep. **4**, 4055 (2014).
[38]T. A. H. Nguyen and A. V. Nguyen, Langmuir **28**, 16725 (2012).
[39]W. Xu and C.-H. Choi, J. Heat Transfer **134**, 051022 (2012).
[40]D. Orejon, K. Sefiane, and M. E. R. Shanahan, Langmuir **27**, 12834 (2011).
[41]B. Bhushan and Y. C. Jung, J. Phys.: Condens. Matter **20**, 225010 (2008).